Molecular dynamics analysis of the influence of Coulomb and van der Waals interactions on the work of adhesion at the solid-liquid interface

Donatas Surblys, Frédéric Leroy, Yasutaka Yamaguchi, and Florian Müller-Plathe
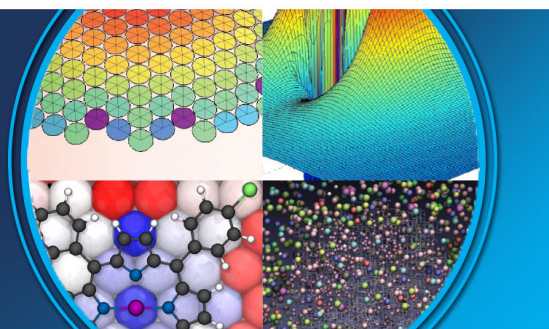
Molecular dynamics analysis of the influence of Coulomb and van der Waals interactions on the work of adhesion at the solid-liquid interface

Donatas Surblys,[1,a)] Frédéric Leroy,[2] Yasutaka Yamaguchi,[1,3,b)] and Florian Müller-Plathe[2]

[1]*Department of Mechanical Engineering, Osaka University, 2-1 Yamadaoka, Suita 565-0871, Japan*
[2]*Eduard-Zintl-Institut für Anorganische und Physikalische Chemie, Technische Universität Darmstadt, Alarich-Weiss-Str. 8, D-64287 Darmstadt, Germany*
[3]*Water Frontier Science and Technology Research Center (W-FST), Research Institute for Science and Technology, Tokyo University of Science, 1-3 Kagurazaka, Shinjuku-ku, Tokyo 162-8601, Japan*

We investigated the solid-liquid work of adhesion of water on a model silica surface by molecular dynamics simulations, where a methodology previously developed to determine the work of adhesion through thermodynamic integration was extended to a system with long-range electrostatic interactions between solid and liquid. In agreement with previous studies, the work of adhesion increased when the magnitude of the surface polarity was increased. On the other hand, we found that when comparing two systems with and without solid-liquid electrostatic interactions, which were set to have approximately the same total solid-liquid interfacial energy, former had a significantly smaller work of adhesion and a broader distribution in the interfacial energies, which has not been previously reported in detail. This was explained by the entropy contribution to the adhesion free energy; i.e., the former with a broader energy distribution had a larger interfacial entropy than the latter. While the entropy contribution to the work of adhesion has already been known, as a work of adhesion itself is free energy, these results indicate that, contrary to common belief, wetting behavior such as the contact angle is not only governed by the interfacial energy but also significantly affected by the interfacial entropy. Finally, a new interpretation of interfacial entropy in the context of solid-liquid energy variance was offered, from which a fast way to qualitatively estimate the work of adhesion was also presented. *Published by AIP Publishing.* https://doi.org/10.1063/1.5019185

I. INTRODUCTION

Since the ground-breaking work of Young in 1805,[1] the behavior of systems with a three-phase contact line, such as droplets, has been a topic of interest both as basic science and in various engineering fields due to its considerable practical importance.[2–4] Owing to recent advances in industrial processes such as high resolution printing[5] and semiconductor production,[6] the resolution of interest has reached the nanometer scale and profound understanding of liquid behavior at such a scale has become more important.

The force balance discussed by Young to describe the shape of a droplet in equilibrium on a given surface takes the following form:[1]

$$\gamma_{lv} \cos\theta - \gamma_{sv} + \gamma_{sl} = 0. \tag{1}$$

Equation (1) relates the contact angle θ to the surface and interfacial tensions of the system, namely, the liquid surface tension γ_{lv}, the solid-vapor interfacial tension γ_{sv}, and the solid-liquid interfacial tension γ_{sl}. Interfacial tension is defined as a partial derivative of free energy as

$$\gamma = \left(\frac{\partial G}{\partial A}\right)_{T,P,N} = \left(\frac{\partial F}{\partial A}\right)_{T,V,N}, \tag{2}$$

where G and F are the Gibbs and Helmholtz free energies, while T, P, V, N, and A represent system temperature, pressure, volume, particle number, and interface area, respectively.

Pioneering works by Kirkwood and Buff on the statistical mechanics of surface tension[7] opened the doors to computational works on the wettability of mono-atomic Lennard-Jones (LJ) liquids governed by short-range forces.[8–15] In many of these works, it was shown that Young's macroscopic model was also applicable to simple mono-atomic liquids at the microscale. Additionally, two of the present authors with other members of their group performed molecular dynamics (MD) simulations to quantify the interfacial tensions in nanometer-sized droplets with realistic models of water-alcohol mixtures on non-polar surfaces. It was demonstrated that Young's equation was also valid in those cases.[16]

The wetting behavior of a given solid-liquid system may also be quantified through the work of adhesion $W_{sl,v}$, which is defined by the work of reversibly removing a given liquid in equilibrium with its vapor from a given solid through

$$W_{sl,v} = \gamma_{sv} + \gamma_{lv} - \gamma_{sl}. \tag{3}$$

Under the condition that γ_{sv} can be approximated by the solid surface tension γ_s as $\gamma_{sv} \approx \gamma_s$, i.e., when the vapor adsorption is negligible,[17] $W_{sl,v}$ is substituted by the solid-liquid work of adhesion W_{sl} as

$$W_{sl} = \gamma_s + \gamma_{lv} - \gamma_{sl}. \tag{4}$$

a)Electronic mail: donatas@gcom.mech.eng.osaka-u.ac.jp
b)Electronic mail: yamaguchi@mech.eng.osaka-u.ac.jp. URL: http://www-gcom.mech.eng.osaka-u.ac.jp/~yamaguchi/.

It was recently shown by MD simulations of water on non-polar and polar surfaces that the effect of vapor adsorption on θ may be considered negligible for systems with $\theta > 60°$.[18] In general, there is a direct connection between the work of adhesion W_{sl} or $W_{sl,v}$ and θ given by the Young-Dupré equation, which for W_{sl} is obtained by combining Eqs. (1) and (4),

$$W_{sl} = \gamma_{lv}\left(1 + \cos\theta\right). \tag{5}$$

Equation (5) shows that the W_{sl} may be obtained through the calculation of γ_{lv} on the one hand and through the measurement of θ in droplet simulations on the other hand. Equation (4) defines W_{sl} as a change in free energy per unit area during the reversible removal process

$$W_{sl} = \left(\frac{\Delta G}{A}\right)_{T,P,N} = \left(\frac{\Delta F}{A}\right)_{T,V,N}, \tag{6}$$

which can be either accessed by calculations of the free energy, e.g., through thermodynamic integration, or obtained directly through interfacial tensions, e.g., through the so-called mechanical route based on the Bakker's equation.[8,9,15,16]

Recently, an approach called the dry-surface method based on thermodynamic integration was developed by two of us to obtain W_{sl} from free energy calculations, i.e., without resorting to droplet simulations.[19] This method was applied to study the wetting behavior of water on various mildly hydrophobic non-polar surfaces like graphite[20] and the basal plane of molybdenum disulfide.[21] In this approach, the solid-liquid pair interactions given in the Lennard-Jones (LJ) form were gradually weakened through a coupling parameter to the point where almost no attractive interaction remained, and the liquid surface was essentially no longer affected by the solid surface. The free energy change per unit area for this transformation is equal to W_{sl} and was obtained by thermodynamic integration along the path defined by the coupling parameter.

In the present work, we extended the dry-surface approach to polar surfaces with Coulomb interactions between liquid and surface in addition to LJ pair interactions. In particular, we performed MD simulations to calculate the solid-liquid work of adhesion between water and a weakly polar, but overall neutral, silica surface without silanol groups, for the sake of simplicity. At its core, the dry-surface method described in this work followed the basic framework of the original dry-surface paper,[19] except for a different integration path because of dealing with Coulomb potential in addition to van der Waals forces. Indeed, as both of them are pair potentials, conceptually there was no need to treat electrostatic interactions differently. Going even deeper, the dry-surface method itself fundamentally used the same methods used for computation of solvation or binding free energies, which have been available in packages such as GROMACS,[22] even offering correct treatment of Coulomb interactions. From this viewpoint, the greatest challenge in applying the dry-surface method to systems with long-range electrostatic interactions at solid-liquid interfaces was rather technical. If done in a straightforward fashion, the dry-surface method would have required to modify the electrostatic solid-liquid interactions without changing solid-solid and liquid-liquid interactions. Within the knowledge of the authors at the time of writing, no MD package offered this when long-range electrostatics were treated with Ewald-based methods, because their default implementations only solve a single Poisson's equation for all system charges and would have required non-trivial modifications to do otherwise. A similar problem existed upon adapting the previously mentioned packages used for computing solvation energies; while the solid-liquid (solute-solvent) interactions can be correctly modified, vacuum (non-periodic) conditions are assumed for decoupled liquid phase (solvent), rendering them inapplicable for work of adhesion computations that require periodic boundary conditions for the liquid phase. Therefore, presently, none of the available tools or packages in their current state can be used to compute the work of adhesion in a straightforward manner for systems such as those in this paper, unless one is ready to take more indirect integration paths.[18] This work offered a method to achieve this through a straightforward integration path with standard molecular dynamics simulations and *a posteriori* computation of solid-liquid energies, provided by readily available and unmodified LAMMPS simulation package.[23] The surface model is described in Sec. II A and specific details of the interaction potential are provided in Sec. II B. Systems used with the dry-surface method are described in Sec. II C, while the extended dry-surface methodology itself is presented in Sec. II D.

During solid-liquid separation process, there is change in both of the LJ and Coulomb components of solid-liquid and liquid-liquid interactions. Regarding the relation between the free energy and the potential energy of solid-liquid interaction, it was shown in Ref. 24 and references therein that the change in liquid-liquid interactions is exactly energy-entropy compensating. In other words, the change in internal energy associated with the changes in liquid-liquid interactions is exactly equal to the change in liquid entropy. As a consequence, W_{sl} depends explicitly only on the *solid-liquid* interactions[24] and is thus expressed by

$$W_{sl} = \Delta u_{sl} - T\Delta s_{sl}, \tag{7}$$

where Δu_{sl} is the increase in the potential energy per unit area due to the solid-liquid interactions upon the solid-liquid separation and Δs_{sl} is the corresponding entropy increase. Because the potential energy is reduced by the solid-liquid contact, Δu_{sl} is positive, meaning that energy, i.e., work must be added to separate the liquid from solid surface. The entropy term $T\Delta s_{sl}$ is also positive as discussed in a previous work.[24] It is also interesting to note that the importance of solute-substrate interactions on entropy was recently discussed in the context of the hydrophobic collapse of macromolecular aqueous systems.[25] We quantified the contribution from both LJ and Coulomb interactions to W_{sl} and showed that for a given value of Δu_{sl}, W_{sl} was larger for pure LJ solid-liquid interactions than for a mixture of LJ and Coulomb interactions. In other words, the presence of interfacial Coulomb interactions induced a larger entropy gain for a given solid-liquid interaction energy upon solid-liquid separation. This is illustrated in Sec. III A, and the underlying mechanisms are discussed in Secs. III B and III C. We also show in Sec. III B that provided that the solid-liquid interactions are dominated by LJ pair interactions, a variety of solid-water systems with solid surfaces extending from graphite, graphene, hexagonal boron nitride, and molybdenum disulfide to the present silica model yielded almost the

same relation between W_{sl} and u_{sl}. Finally, an approach to estimate $T\Delta s_{sl}$ with a minimal calculation cost is proposed in Sec. III D.

Altogether, the present contribution sheds light on the mechanisms at the molecular level that determine the magnitude of entropy effects on polar and non-polar surfaces.

II. METHODOLOGY

The LAMMPS[23] MD package was used to perform the simulations with the velocity Verlet time integrator. As the O–H bond of selected water model had a vibration period of approximately 9 fs, a timestep of 0.5 fs was chosen according to the general rule of picking below one-tenth of the fastest motion period.[26] It was also confirmed that the properties of water bulk were properly reproduced under constant-temperature ensembles mentioned below. The positions of the particles were collected every 200 steps.

A. Silica surface

Silica surface was modeled as α-cristobalite, where water was in contact with its $(10\bar{1})$ plane. The model from the work of Emani *et al.*[27] was used to create the surface, as will be discussed in detail below. With this model, harmonic potentials were employed to describe the bending motion of the Si–O–Si and O–Si–O angles, as well as the vibrations of the Si–O bonds. For the free energy and droplet calculations, the relaxed surface was used, with the atoms frozen at their equilibrium position. The potential parameters for the flexible silica model are given in Table I.

As will be discussed later in Sec. II B, we used cut-off lengths and potential truncation schemes different from those in the original paper by Emani *et al.*[27] Therefore, simulations of a silica bulk were performed first to recalculate the unit cell parameters to avoid unwanted stress in the structure. The coordinates of an α-cristobalite cell containing 12 Si and 24 O atoms with the dimension $8.55 \times 4.98 \times 12.14$ Å^3 and the $(10\bar{1})$ plane aligned perpendicular to the z-direction were obtained from the supplementary material of Ref. 27. This "basic cell" was used as a building block to create bulk silica systems. Two bulk systems were constructed from $4 \times 7 \times 3$ and

TABLE I. Lennard-Jones parameters and electrostatic charges for water and silica. Equilibrium distances, angles, and force constants for the harmonic potentials for the water and silica models are also included.

Atom	σ (Å)	ε (kcal/mol)	q (e)
O(water)	3.1655	0.155 43	−0.82
H	...	...	+0.41

Atom	σ (Å)	ε (kcal/mol)	q (e)
O(SiO$_2$)	3.47	0.054	−0.55
Si	4.15	0.093	+1.10

Bond	r_0 (Å)	k_r (kcal/mol Å^2)	
O–H	1.012	529.581	
Si–O	1.68	285	

Angle	θ_0 (deg)	k_θ (kcal/mol rad^2)	
O–Si–O	109.5	100	
Si–O–Si	149	100	

$6 \times 10 \times 4$ basic cells with 3024 and 8640 atoms, respectively. A simulation with constant number of particles, constant pressure, and constant temperature (*NPT*) was performed for each system with periodic boundary conditions in all directions. A temperature of 300 K and zero pressure were maintained by Nosé-Hoover style equations,[28] with the thermostat and barostat each having three chains and damping coefficients set to 50 and 500 fs, respectively. The cell dimensions in the x-, y- and z-directions were independently controlled because of the anisotropic nature of the cell. The systems were equilibrated for 0.5 ns, and another 0.5 ns was used to calculate the mean dimensions of the cell. The small and large bulk systems yielded similar dimensions of the equilibrated structures, namely, $8.57 \times 4.96 \times 12.16$ Å^3 for the dimension of the basic cell.

A silica surface was prepared by first creating a bulk system consisting of $4 \times 7 \times 2$ basic cells, followed by breaking the bonds that crossed the boundary of the initial simulation cell in the z-direction, and finally by elongating the z-dimension of the simulation domain to 200 Å. The boundary condition was also changed from periodic to mirror in this direction. Oxygen atoms with a dangling bond were repositioned to be bonded to two silica atoms at the surface, creating siloxane bridges. A simulation with constant number of particles, constant volume, and constant temperature (*NVT*) followed, where the temperature was set to 300 K using the Langevin thermostat[29] with a damping coefficient of 1 ps. The system was first equilibrated for 1.1 ns. The mean positions of the silica atoms were obtained from an additional simulation of 1 ns, during which the periodicity of the silica crystal structure in the x- and y-directions was taken into account. These mean positions were used to create a silica surface with frozen atoms, as can be seen in panel (a) of Fig. 1. Note that the crystal structure was deformed next to the surface. This deformation caused not only the surface but also the whole silica crystal to expand by roughly 11% in the z-direction compared with bulk silica. We also note that the silica slab is overall neutral.

B. Interaction potentials

The flexible SPC/Fw[30] model was chosen to represent water because this model was reported to yield good agreement with the experimental data for dynamical and dielectric properties.[31] The bond vibrations and angle bending motion were modeled by harmonic potentials. The flexibility of the model enables the water molecule to change its dipole moment, which was considered to be more suitable than rigid models for the investigation of the interaction with a polar surface. The parameters of the water model are summarized in Table I.

Water and the silica surface interacted through the LJ and Coulomb pair potentials. Because these potentials are independent of each other, the total solid-liquid interaction potential energy Φ_{sl} is the sum of the LJ $\Phi_{sl(LJ)}$ and Coulomb $\Phi_{sl(C)}$ components. In the original dry-surface calculations that led to W_{sl}, the interaction strength between water and surface was varied between the full interaction and a value such that water and surface were virtually uncoupled. In this work, the variation was implemented through two coupling parameters $\kappa(>0)$
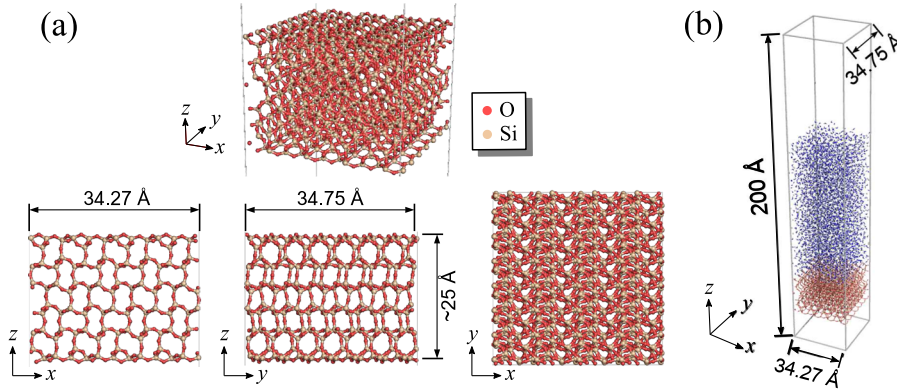
(a)

(b)

FIG. 1. (a) Top and side views of the silica surface used in film systems. The silica surface consisted of only silicon and oxygen atoms and had no silanol groups. (b) Side view of one of the film systems composed of a silica surface and a water liquid layer, which were used for the dry-surface method. Oxygen atoms of water molecules are colored blue for clarity. The atomic positions of the silica surface were fixed.

and $\lambda (\geq 0)$ by

$$\Phi_{sl} = \Phi_{sl(LJ)}(\kappa) + \Phi_{sl(C)}(\lambda). \qquad (8)$$

The dependence of $\Phi_{sl(LJ)}$ on κ was given by the following:

$$\Phi_{sl(LJ)}(\kappa) = \kappa \sum_{i \in water} \sum_{j \in SiO_2} 4\sqrt{\varepsilon_i \varepsilon_j} \left[\left(\frac{\sigma_{ij}}{r_{ij}} \right)^{12} - \left(\frac{\sigma_{ij}}{r_{ij}} \right)^{6} \right], \quad (9)$$

where ε_j is either $\varepsilon_{O(SiO_2)}$ or ε_{Si} given in Table I and r_{ij} is the distance between the ith water atom and jth surface atom. The distance parameters between different atom types σ_{ij} were obtained through the Lorentz-Berthelot mixing rule, i.e., arithmetic mean. The dependence of $\Phi_{sl(C)}$ on λ was also modeled with a linear relationship given by the following:

$$\Phi_{sl(C)}(\lambda) = \lambda \sum_{i \in water} \sum_{j \in SiO_2} \frac{q_i q_j}{4\pi \epsilon_0 r_{ij}}, \qquad (10)$$

where q_j is either $q_{O(SiO_2)}$ or q_{Si} given in Table I. The intervals for the variation of κ and λ are discussed in Sec. II D.

The switching function often employed in the Chemistry at HARvard Molecular Mechanics (CHARMM) force field[32] was applied to the LJ potential between 12 and 13 Å such that the potential vanished at 13 Å. Note that the force switching function also used in CHARMM was not employed; i.e., the LJ force $F_{i(LJ)}$ applied to particle i in this study is the strict derivative of the potential energy

$$F_{i(LJ)} = -\frac{\partial S^{pot}\Phi_{LJ}}{\partial r_i} = -S^{pot}\frac{\partial \Phi_{LJ}}{\partial r_i} - \Phi_{LJ}\frac{\partial S^{pot}}{\partial r_i}, \qquad (11)$$

where S^{pot} is the CHARMM potential switching function. In principle, S^{pot} should also be included in Eq. (9) but was omitted for clarity. Coulomb interactions were calculated using the charges in Table I with the long-range electrostatic interactions treated by the Particle-Particle-Particle-Mesh (PPPM) method[33] with a relative force accuracy set to 10^{-6} and a real space cut-off distance set to 13 Å. By default, the PPPM method treats systems as periodic in all directions, which makes unnecessary electrostatic interactions appear between real and replica simulation cells in the z-direction for our non-bulk systems. To remedy this, the "slab" option was used with LAMMPS "kspace_modify" command, which effectively removed these unwanted interactions by disabling dipole-dipole interaction with the replica images in the z-direction and by elongating system dimensions by 3 times only during the calculation of electrostatics, effectively creating more empty space between real and replica images.[34]

C. Simulation conditions

The free energy calculations with the dry-surface method were carried out for a water film adsorbed on the silica surface. A snapshot of such a simulation setup is shown in panel (b) of Fig. 1. The liquid film consisting of 3600 molecules was placed on the top of the silica described in Sec. II A. Simulations at *NPT* conditions were performed, where the positions of silica atoms were fixed and the temperature of the liquid phase was kept at 300 K by stochastic velocity rescaling[35] with a damping coefficient of 1 ps. This thermostat was chosen because it is known to reproduce the correct diffusive behavior of water molecules regardless of the damping coefficient.[36] For systems with very weak solid-liquid interactions ($\kappa \leq 0.1$, $\lambda = 0$), the total translational momentum of the water molecules in the z-direction was set to zero every 10^4 timesteps to prevent the liquid film from drifting away from the silica surface. These weak-interaction systems were equilibrated for 10 ns owing to high density fluctuation at the solid-liquid interface and slower equilibration due to removal of linear momentum, while the rest of the systems were equilibrated for 1 ns. The dry-surface method and related analyses were carried out with the simulation time depending on the type of solid-liquid interactions in the system as follows: 5 ns for very weak solid-liquid interactions ($\kappa \leq 0.1$, $\lambda = 0$), 3 ns for weak solid-liquid interactions ($0.1 < \kappa \leq 1$, $\lambda = 0$), and 1.5 ns for the remaining systems. The equilibration times were deemed to be enough for these systems because water molecules have a high diffusion coefficient. The convergence of the potential energy with time was also verified.

D. Dry-surface calculations

The dry-surface methodology[19–21] is a thermodynamic integration[37] approach used to obtain W_{sl} as the free energy difference per unit area between the actual solid-liquid system with the interfacial tension γ_{sl} and a reference system whose interfacial tension is close to $\gamma_s + \gamma_{lv}$. In practice, the actual interface is turned into the reference interface by quasi-statically modifying the solid-liquid pair interaction potentials with the aim to decrease the depth of the total solid-liquid interaction potential. In the present study, W_{sl} for the original silica-water surface with $(\kappa, \lambda) = (1, 1)$ was obtained by reversibly changing (κ, λ) into $(\kappa_0, 0)$ with $\kappa_0 \ll 1$. Note that values for (κ, λ) different from $(1, 1)$ describe systems whose surface has the structure of silica but whose solid-liquid

interaction strength is either larger or lower than the actual interaction. Also note that for W_{sl} as a two-variable function of κ and λ, an arbitrary system satisfying $W_{sl}(\kappa, \lambda) = W_{sl}(1, 1)$ with $(\kappa, \lambda) \neq (1, 1)$ is possible, e.g., by decreasing the LJ interactions with $\kappa < 1$ and simultaneously increasing the Coulomb interactions with $\lambda > 1$. This is illustrated later in the text.

The "slab" treatment of electrostatics, discussed in Sec. II B, requires a non-periodic condition in the z-direction, which greatly limits pressure control options available in LAMMPS. Because of this, a setup of liquid films in equilibrium with their vapor adsorbed on solid surfaces was chosen instead of one where the liquid files are positioned between two outer surfaces,[19] as having a vapor phase freed us from the need of a barostat. The film systems contained a constant number of particles in a fixed volume, and temperature was also maintained constant. Hence, the solid-liquid work of adhesion at a given (κ, λ) is the Helmholtz free energy difference per unit area expressed by

$$W_{sl}(\kappa, \lambda) = -\frac{1}{A}\left[F(\kappa, \lambda) - F(\kappa_0, 0)\right], \qquad (12)$$

where A is the area of xy cross-section of the simulation system parallel to the surface. Equation (12) is independent of the path, and an important constraint to correctly calculate the thermodynamic integration and obtain W_{sl} in a reliable way is to quasi-statically trace an arbitrary path between the given state (κ, λ) and the reference state $(\kappa_0, 0)$. Note that strictly speaking, the convergence of Eq. (12) does depend on the integration path. In the present study, a satisfactory convergence was obtained with an integration that was performed in two phases: in the first phase, called LJ modification phase (LJ-mp), the change from $(\kappa_0, 0)$ to $(\kappa, 0)$ was performed, and in the second phase, called Coulomb modification phase (C-mp), the change from $(\kappa, 0)$ to (κ, λ) was performed. Note that the C-mp was newly implemented in the present study as an extension of the previous dry-surface methodology only with the LJ-mp operation. Additional calculations were performed for systems with $\lambda = 0$ and $1 < \kappa < 2$ as well as $1 < \lambda < 2$ and $\kappa = 1$, i.e., systems with stronger solid-liquid LJ interaction without Coulomb interactions and those with stronger solid-liquid Coulomb interaction with keeping the LJ strength. With these variations, it was possible to compare systems with the same average solid-liquid interfacial potential energy but with a different balance of the LJ and Coulomb interactions and thus possible to address the effects of these respective interactions on the work of adhesion.

Because the LJ and Coulomb potentials are additive contributions to Φ_{sl} and also because the system Hamiltonian explicitly depends on κ and λ [Eqs. (9) and (10)], for the present thermodynamic path consisting of LJ-mp and C-mp, the free energy difference is

$$F(\kappa, \lambda) - F(\kappa_0, 0) = \int_{\kappa_0}^{\kappa} \left\langle \frac{\partial \Phi_{sl(LJ)}(\kappa')}{\partial \kappa'} \right\rangle_{T,V,N,\lambda=0} d\kappa'$$
$$+ \int_0^\lambda \left\langle \frac{\partial \Phi_{sl(C)}(\lambda')}{\partial \lambda'} \right\rangle_{T,V,N,\kappa} d\lambda'. \qquad (13)$$

The analytical forms of the partial derivatives in Eq. (13) are given by

$$\frac{\partial \Phi_{sl(LJ)}}{\partial \kappa} = \Phi_{sl(LJ)}(1) \qquad (14)$$

and

$$\frac{\partial \Phi_{sl(C)}}{\partial \lambda} = \Phi_{sl(C)}(1), \qquad (15)$$

respectively. Equations (14) and (15) mean that the integrands in Eq. (13) are obtained from the analytical expression of the water-silica potential energies with (κ, λ) set equal to $(1, 1)$ but with the configuration space accessible at other values of (κ, λ). We further introduced the quantities $u^0_{sl(LJ)} = \Phi_{sl(LJ)}(1)/A$ and $u^0_{sl(C)} = \Phi_{sl(C)}(1)/A$ for the integrands of Eq. (12). Note that both $u^0_{sl(LJ)}$ and $u^0_{sl(C)}$ depend implicitly on κ and λ. The operational equation for W_{sl} is thus

$$W_{sl}(\kappa, \lambda) = -\int_{\kappa_0}^{\kappa} \left\langle u^0_{sl(LJ)} \right\rangle_{T,V,N,\lambda=0} d\kappa'$$
$$- \int_0^\lambda \left\langle u^0_{sl(C)} \right\rangle_{T,V,N,\kappa} d\lambda'. \qquad (16)$$

Molecular dynamics was used to calculate the ensemble averages of the integrand in Eq. (16) and the integrals were subsequently calculated via the trapezoidal rule. In practice, the calculated ensemble averages were substituted by the time averages of the quantities in the bracket, given, for instance, by

$$\left\langle u^0_{sl} \right\rangle \approx \overline{u^0_{sl}} \equiv \frac{1}{t^{sim}} \int_0^{t^{sim}} u^0_{sl} dt, \qquad (17)$$

using the simulation time t^{sim} and assuming that the system was ergodic. A total number of 33 and 31 data points were used for LJ-mp and C-mp, respectively. The $\overline{u^0_{sl}}$ for very weak, weak, and normal solid-liquid interaction systems took at most approximately 3, 2, and 0.8 ns to converge, respectively, with the greatest standard error of the mean at 0.2 mN/m, obtained by using 500 sample block averages.

A challenging part of the present method is to calculate the Coulomb components of solid-liquid interaction energy as they are long-ranged forces. This was treated by employing the "group/group" command in LAMMPS, which calculates the potential energy between two atom groups. Most importantly, the long-ranged Coulomb interactions are treated correctly, as, in the case of the PPPM method, additional charge meshes are produced for each atom group and extra FFTs are performed by LAMMPS to obtain exact interaction energies. The only constraint is that at least one of the atom groups must be neutral, which in our case was valid for both silica and water films. By using existing trajectories with the "rerun" command and modified parameter files, we obtained the Hamiltonian derivatives in Eqs. (14) and (15).

III. RESULTS AND DISCUSSION

A. Work of adhesion

Figure 2 shows the average of the Hamiltonian derivatives $\overline{u^0_{sl(LJ)}}(\kappa, \lambda)$ and $\overline{u^0_{sl(C)}}(\kappa, \lambda)$ together with the work of adhesion $W_{sl}(\kappa, \lambda)$ calculated, respectively, according to Eqs. (14)–(16), where the left and right panels correspond to the LJ-mp and
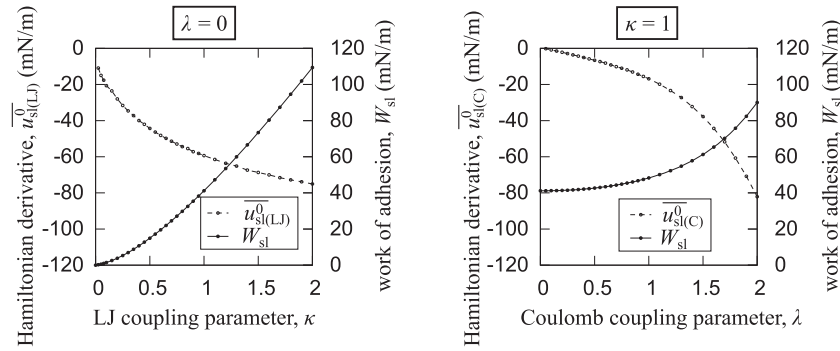
FIG. 2. Average of Hamiltonian derivatives $u^0_{\text{sl(LJ)}}(\kappa, \lambda)$ and $u^0_{\text{sl(C)}}(\kappa, \lambda)$ in Eqs. (14) and (15) and solid-liquid work of adhesion $W_{\text{sl}}(\kappa, \lambda)$ in Eq. (16) in relation to the change in Lennard-Jones (LJ) and Coulomb (C) coupling parameters (κ, λ) for (left) $(0, 0) \rightarrow (\kappa, 0)$ and (right) $(1, 0) \rightarrow (1, \lambda)$. The work of adhesion $W_{\text{sl}}(1, 0)$ in the left panel was used as the initial value for the right panel. Error bars for $u^0_{\text{sl(LJ)}}(\kappa, \lambda)$ and $u^0_{\text{sl(C)}}(\kappa, \lambda)$ are not shown due to the small size of the standard error of the mean, which is at most 0.2 mN/m.

C-mp of $(\kappa_0, 0) \rightarrow (\kappa, 0)$ and $(1, 0) \rightarrow (1, \lambda)$, respectively. The value of $\overline{u^0_{\text{sl(LJ)}}}(\kappa_0, 0)$ at the lower limit of integral in Eq. (16) was obtained by extrapolating from the two nearest data points in the left panel of Fig. 2. Note that even at weak Coulomb interaction during C-mp, the Hamiltonian derivative had a small value of $\overline{u^0_{\text{sl(C)}}}(1, 0) \approx 0.5$ mN/m, though it is too small to be seen from the right panel of Fig. 2. This was likely because at $\lambda = 0$, there was very little correlation between the heterogeneous electrostatic field created by the silica surface and water molecule orientations, which resulted in a cancelled out Coulomb gross potential.

It is difficult to determine the precision of the numerical integration, but it is thought to be acceptably small taking into account the small size of the standard error of the mean of the Hamiltonian derivatives and the smooth distribution of data points in Fig. 2. The work of adhesion for the LJ-mp in the left panel had the same basic shape as reported by Leroy and Müller-Plathe[19]; i.e., the graph became more linear at larger κ. On the other hand, unlike the left panel, the work of adhesion for the C-mp shown in the right panel did not appear to become linear at larger λ but showed a more parabolic shape. In either case, the work of adhesion increased with strengthening of the solid-liquid interaction as expected. This would result in increasing wettability, i.e., a decreasing contact angle.

B. Relation between the average total solid-liquid energy, entropy, and work of adhesion

Because the thermodynamic integration in this work is performed in the opposite direction compared with that described by Eq. (7) and since solid-liquid interaction energy is approximately zero at $(\kappa = \kappa_0, \lambda = 0)$, the relation between work of adhesion, solid-liquid energy, and entropy change can be written as

$$W_{\text{sl}}(\kappa, \lambda) \approx -\overline{u_{\text{sl}}}(\kappa, \lambda) + T\Delta s_{\text{sl}}(\kappa, \lambda), \quad (18)$$

where average total solid-liquid energy per unit is

$$\overline{u_{\text{sl}}}(\kappa, \lambda) = \left[\overline{u_{\text{sl(LJ)}}}(\kappa, \lambda) + \overline{u_{\text{sl(CL)}}}(\kappa, \lambda)\right] \quad (19)$$

and the entropy difference per unit area is

$$\Delta s_{\text{sl}}(\kappa, \lambda) = s_{\text{sl}}(\kappa, \lambda) - s_{\text{sl}}(\kappa_0, 0). \quad (20)$$

In addition, because of the chosen integration direction, Δs_{sl} is always negative and "entropy *loss*" will be used to describe the entropy component ΔTs_{sl}, as opposed to "entropy *gain*," except when explicitly referring to the process of liquid separation from solid. The value of $\overline{u_{\text{sl}}}$ in Eq. (19) can be calculated using the LAMMPS "group/group" command in the same manner as used for the Hamiltonian derivatives in Eqs. (14) and (15). Hence, $T\Delta s_{\text{sl}}$ is obtained by the following:

$$T\Delta s_{\text{sl}} \approx W_{\text{sl}} + \overline{u_{\text{sl}}}. \quad (21)$$

The left panel of Fig. 3 shows the relation between the average total solid-liquid energy $-\overline{u_{\text{sl}}}$ and work of adhesion W_{sl} for the present LJ-mp with (κ, λ) varied from $(\kappa_0, 0)$ to $(2, 0)$ together with the data from previous studies.[20] A dashed line of $W_{\text{sl}} = -\overline{u_{\text{sl}}}$ was superimposed for reference. A nearly perfect match between the present and the previous data was observed, indicating the same basic relation between the work of adhesion and the solid-liquid energy held in case of LJ-only solid-liquids interactions, regardless of surface structures or water models.[20] In addition, the comparison with the dashed line indicates that the entropy in Eq. (18) had negative contribution to the work of adhesion; i.e., $T\Delta s_{\text{sl}}(\kappa, \lambda) < 0$.

The right panel of Fig. 3 shows the relations between W_{sl} and $-\overline{u_{\text{sl}}}$ as well as between entropy loss $-T\Delta s_{\text{sl}}$ and $-\overline{u_{\text{sl}}}$ for LJ-mp and C-mp in the present study, where (κ, λ) is varied from $(1, 0)$ to $(1, 2)$ for the C-mp. A linear dependence of W_{sl} on $-\overline{u_{\text{sl}}}$ was seen for both phases when the solid-liquid energy was large, and as a consequence, $-T\Delta s_{\text{sl}}$ also linearly depended on $-\overline{u_{\text{sl}}}$; however, the slopes were different for the two phases.

We appended linearly fitted lines to the points of W_{sl} for the LJ-mp from $(\kappa, \lambda) = (1, 0)$ to $(2, 0)$ and those for the C-mp from $(\kappa, \lambda) = (1, 0)$ to $(1, 2)$, which approximated

$$-\frac{W_{\text{sl}}(\kappa, 0) - W_{\text{sl}}(1, 0)}{\overline{u_{\text{sl}}}(\kappa, 0) - \overline{u_{\text{sl}}}(1, 0)} \approx \text{const.} \quad (1 \le \kappa \le 2) \quad (22)$$

and

$$-\frac{W_{\text{sl}}(1, \lambda) - W_{\text{sl}}(1, 0)}{\overline{u_{\text{sl}}}(1, \lambda) - \overline{u_{\text{sl}}}(1, 0)} \approx \text{const.} \quad (1 \le \lambda \le 2), \quad (23)$$
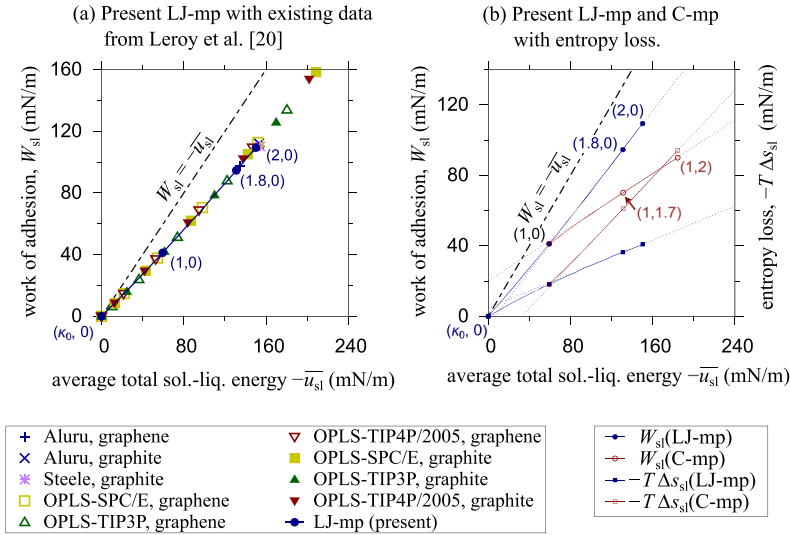
FIG. 3. (a) Work of adhesion W_{sl} versus average total solid-liquid energy per unit area $-\overline{u_{sl}}$ for present data of the LJ modification phase (LJ-mp) with the existing data from the work of Leroy *et al.*,[20] where some data points are omitted for clarity. (b) Work of adhesion W_{sl} and entropy loss $-T\Delta s_{sl}$ per unit area versus $-\overline{u_{sl}}$ for the present data of LJ-mp and Coulomb modification phase (C-mp). The results of linear fittings are shown in Table II. Corresponding values of (κ, λ) are shown for several points in both the graphs.

respectively. The slopes of the lines are summarized in Table II with the corresponding slopes for the relation between $-T\Delta s_{sl}$ and $-\overline{u_{sl}}$. The comparison of the slopes for $-T\Delta s_{sl}$ between LJ-mp and C-mp indicates that a greater entropy loss occurred upon increasing the silica charges. This difference is thought to be because the electrostatic forces from the silica surface additionally constrained the orientation of the water molecules at the solid-liquid interface, causing different tendencies in the entropy change and water structure.

C. Properties of water adsorption layer at the solid-liquid interface

It was expected that the different slopes mentioned in Sec. III B in Fig. 3 and Table II came from the different structures of liquid at the solid-liquid interface in LJ-mp and C-mp. We investigated the microscopic details of the adsorption layer. Figure 4 shows the density distribution of water near the solid surface for various (κ, λ) along the LJ-mp and C-mp for (κ, λ) from $(\kappa_0, 0)$ to $(2, 0)$ and from $(1, 0)$ to $(1, 2)$. The density in Fig. 4 was calculated using the point mass at the oxygen and hydrogen sites of water molecules. The peaks and dips in the density distribution were simply amplified with the increase in κ for the LJ-mp at $\kappa \geq 1$, with the position of two adsorption layers with high density remaining unchanged, whereas the adsorption layer adjacent to the solid-liquid interface approached the solid surface with the increase in λ for the C-mp.

We further examined the properties of the first adsorption layer, which is set approximately as the initial 0.4 nm from the silica surface for all systems and indicated by a dashed line in Fig. 4. Although this was a somewhat rough approximation,

as the positions of density peaks and dips differed for different systems, it was verified that slight variation of the adsorption layer boundary did not influence the overall results and a more rigid and systematic definition would have been difficult to apply for systems with very weak solid-liquid interactions, because no distinct density peaks existed, illustrated by $(\kappa_0, 0)$ in Fig. 4. The area number density of the first adsorption layer is defined as

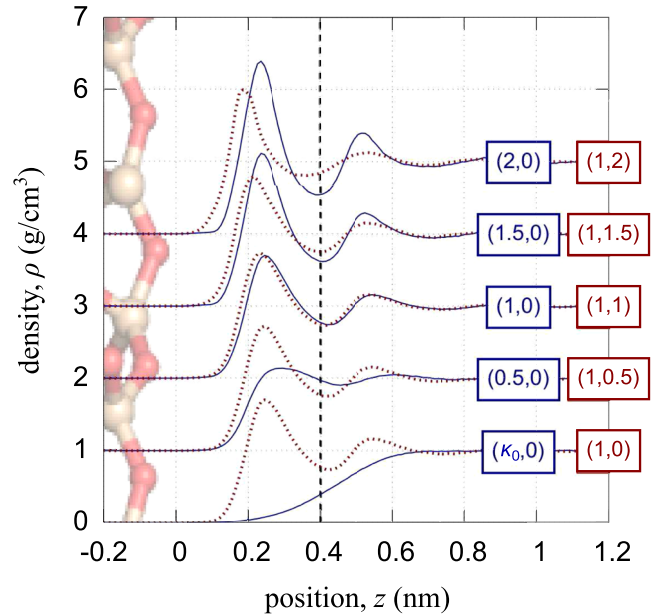$$n^{\text{ads}} \equiv \left\langle \frac{N^{\text{ads}}}{A} \right\rangle, \tag{24}$$

FIG. 4. Density distribution of water at the solid-liquid interface of systems with various LJ and Coulomb parameters (κ, λ) along (blue solid lines) LJ-mp from $(\kappa_0, 0)$ to $(2, 0)$ with $\lambda = 0$ and (red dotted lines) C-mp from $(1, 0)$ to $(1, 2)$ with $\kappa = 1$. The origin of position z is set to be at approximately the silica surface. The density was calculated using the point mass at the oxygen and hydrogen sites of water molecules, and the graph lines were increasingly shifted by 1 g/cm³ for clarity. A snapshot of the silica surface is superimposed to the scale of the position axis. The area of first adsorption layer for the analysis in Figs. 5 and 6 was defined at $z < 0.4$ nm, marked by a vertical gray dashed line.

TABLE II. Slopes of linearly fitting lines in the left panel of Fig. 3 given by Eqs. (22) and (23).

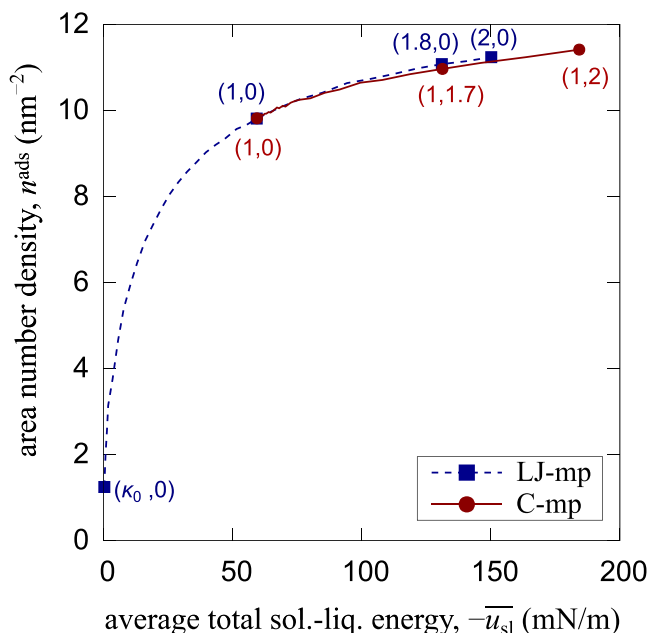| Mod. phase	Fitting range of (κ, λ)	Slope for W_{sl}	Slope for $-T\Delta s_{sl}$
LJ	$(1, 0) \rightarrow (2, 0)$	0.76	0.24
Coulomb	$(1, 0) \rightarrow (1, 2)$	0.38	0.62

FIG. 5. Area number density of the first adsorption layer n^{ads} at the solid-liquid interface as a function of the average total solid-liquid energy $-\overline{u_{\text{sl}}}$. The coupling parameters (κ, λ) were varied from $(\kappa_0, 0)$ to $(2, 0)$ and from $(1, 0)$ to $(1, 2)$ for the LJ-mp and C-mp, respectively. Two systems at $(\kappa, \lambda) = (1.8, 0)$ and $(1, 1.7)$ with roughly the same $-\overline{u_{\text{sl}}}$ are compared in the left panel of Fig. 6. Corresponding values of (κ, λ) are shown for several points.

where N^{ads} indicates the number of water molecules inside the first adsorption layer. Figure 5 shows this area number density plotted against the average total solid-liquid energy $-\overline{u_{\text{sl}}}$. Surprisingly, the values of n^{ads} at a given solid-liquid energy were almost the same for LJ-mp and C-mp, and their increase with the increase in the average total solid-liquid energy $-\overline{u_{\text{sl}}}$ seemed to saturate for larger $-\overline{u_{\text{sl}}}$. However, this does not mean that the water structure at the interface was the same, as already inferred from the comparison of the topmost density distributions shown in Fig. 4 from $(\kappa, \lambda) = (2, 0)$ and $(1, 2)$. In addition, even though the density peak for $(\kappa, \lambda) = (2, 0)$ in Fig. 4 was higher than that for $(\kappa, \lambda) = (1, 2)$, the area number density n^{ads} for the former was lower than that for the latter in Fig. 5, which also indicated the difference in the structure of water at the interface.

To extract the difference in the microscopic structure of water at the solid-liquid interface, distributions of the dipole orientation of water molecules there were analyzed. The left

panel of Fig. 6 shows the probability density functions of cosine of the angle α between the water dipole vector and the outward surface normal of the silica surface for systems at $(\kappa, \lambda) = (1.8, 0)$ and $(1, 1.7)$. The two systems had roughly the same average total solid-liquid energy of about 131 mN/m and area number density as shown in Fig. 5, while the work of adhesion was different at 94.6 and 70.2 mN/m, respectively, in Fig. 3. Note that in order to exactly capture the molecular orientation, multi-dimensional distribution functions using two or three characteristic vectors were needed.[38,39] However, the present definition was chosen because of its simplicity and the fact that the dipole orientation inside bulk produces an uniform distribution. In both the systems, the average dipole cosine was slightly above zero; i.e., water dipole was directed slightly toward the liquid phase from the horizontal plane. The main difference was observed in the dispersion of the peaks: the system of $(\kappa, \lambda) = (1, 1.7)$ with solid-liquid Coulomb interaction had a wider distribution than the system with only LJ interaction between solid and liquid.

Since a single dominant peak was observed in the probability density function as in the left panel of Fig. 6, the dispersion was examined through its standard deviation given by

$$\sigma(\cos \alpha) \equiv \sqrt{\overline{\cos^2 \alpha} - \overline{\cos \alpha}^2}. \tag{25}$$

The right panel of Fig. 6 shows the standard deviation $\sigma(\cos \alpha)$ plotted against the average total solid-liquid energy $-\overline{u_{\text{sl}}}$, where the overbar denotes the time and molecular average. The dispersion was clearly different for systems along the LJ-mp and C-mp, which showed positive and negative correlation with $-\overline{u_{\text{sl}}}$, respectively. This can be explained as follows: the silica had both positively and negatively charged atoms at the surface, which created a heterogeneous electric field, and the preferable dipole orientation of water molecules depended on the location at the surface; hence, this local electric field was strengthened by increasing the Coulomb interaction, which then resulted in the broadening of the dipole distribution. On the other hand, by only increasing the LJ interaction between solid and liquid, water molecules were simply confined more in the first adsorption layer without change in the preference in the dipole orientation. This difference is also closely related to the difference in the dependence of entropy loss on the average total solid-liquid energy along the LJ-mp and C-mp shown in Fig. 3 and Table II.
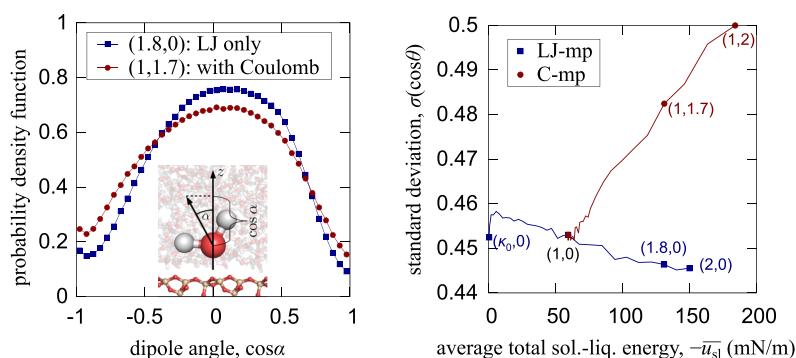

FIG. 6. (Left) probability density function of the cosine of dipole orientation $\cos \alpha$ of water molecules in the first adsorption layer for two systems of $(\kappa, \lambda) = (1.8, 0)$ and $(1, 1.7)$ with roughly the same solid-liquid energy but with different work of adhesion. The angle α was set as the angle between the water dipole vector and the outward normal of the silica surface. (Right) standard deviation $\sqrt{\overline{\cos^2 \alpha} - \overline{\cos \alpha}^2}$ of $\cos \alpha$ as a function of the average total sol.-liq. energy $-\overline{u_{\text{sl}}}$. Corresponding values of (κ, λ) are shown for several points.

It might be tempting to directly link the difference in the standard deviation of dipole dispersion in the right panel of Fig. 6 to the difference in entropy loss between the two integration phases. Indeed, for a normal distribution, the Shannon entropy is proportional to the standard deviation,[40] and a similar relation would hold for our systems as there is only one dominant peak in the distribution. Unfortunately, this is not the case because the process of increasing solid-liquid interaction strength would on the one hand result in a slight entropy loss for the LJ-mp and on the other hand indicate an entropy gain in the C-mp. This is very different from what we have observed in Fig. 3 and Table II; both systems showed entropy loss, with C-mp resulting in a larger entropy change. The reasons for this are multifold. As will be discussed in Sec. III D, entropy change can be interpreted as a function of energy fluctuations of the solid-liquid energy. Figure 6 only reflects the distribution of the orientation of water molecules, and it lacks the information reflecting energy values, such as the coupling parameters or the position of the adsorption layer, as shown in Fig. 4. This is especially substantial for the LJ-mp phase as the hydrogen atoms of the water model used are no longer interacting with the silica surface; i.e. a change in rotational orientation has a much smaller effect on the energy value. The information about the fluctuation of molecule orientation is also missing in Fig. 6; e.g. an interfacial molecule fixed at a certain orientation and one fluctuating between two different orientations could produce identical distributions of dipole orientation and still have substantially different entropies. Finally, other absorption layers besides the first one might also have a significant contribution to the solid-liquid entropy, and indeed, conditions where water molecules in the first adsorption layer had significantly slower dynamics have been observed.[39] All these reasons prevent a straightforward connection between the dipole orientations and the change in the solid-liquid entropy.

D. Entropy and energy variance

In light of a great discrepancy between the solid-liquid entropy and dipole orientation of interfacial water molecules described in Sec. III C, we looked for a better way to gauge the entropy change and took a closer look at how to calculate entropy. Following the same train of thought as thermodynamic integration applied to the calculation of free energy change, the entropy change via (κ, λ) was expressed by[41,42]

$$T\Delta s_{sl} \equiv T\left[s_{sl}(\kappa, \lambda) - s_{sl}(\kappa_0, 0)\right]$$
$$= \frac{A}{k_B T}\left[\int_{\kappa_0}^{\kappa}\left(\overline{\frac{\partial u_{sl}(\kappa', 0)}{\partial \kappa'} \cdot u_{sl}(\kappa', 0)} - \overline{\frac{\partial u_{sl}(\kappa', 0)}{\partial \kappa'}}\,\overline{u_{sl}(\kappa', 0)}\right)d\kappa' + \int_0^{\lambda}\left(\overline{\frac{\partial u_{sl}(\kappa, \lambda')}{\partial \lambda'} \cdot u_{sl}(\kappa, \lambda')} - \overline{\frac{\partial u_{sl}(\kappa, \lambda')}{\partial \lambda'}}\,\overline{u_{sl}(\kappa, \lambda')}\right)d\lambda'\right],$$
$$(26)$$

where k_B is the Boltzmann constant, and ergodic nature of the system exemplified in Eq. (17) is assumed as well. Hereafter, obvious corresponding variables (κ, λ) of u_{sl} will be occasionally omitted for simplicity. We further expanded this equation using Eqs. (14) and (15) as

$$T\Delta s_{sl} = \frac{A}{k_B T}\left[\int_{\kappa_0}^{\kappa}\left(\overline{u_{sl(LJ)}^0 \cdot \overline{u_{sl}}} - \overline{u_{sl(LJ)}^0 \cdot u_{sl}}\right)_{\lambda=0}d\kappa' + \int_0^{\lambda}\left(\overline{u_{sl(C)}^0 \cdot \overline{u_{sl}}} - \overline{u_{sl(C)}^0 \cdot u_{sl}}\right)_{\kappa}d\lambda'\right]; \quad (27)$$

hence, the entropy change could be obtained by numerically integrating the RHS. In addition, by using the relation

$$u_{sl}(\kappa, \lambda) = u_{sl(LJ)} + u_{sl(C)}$$
$$= \kappa u_{sl(LJ)}^0 + \lambda u_{sl(C)}^0, \quad (28)$$

the LJ and Coulomb contributions to the entropy effect in Eq. (27) were divided as

$$T\Delta s_{sl} = T\Delta s_{sl(LJ)} + T\Delta s_{sl(C)}. \quad (29)$$

It followed for the LJ contribution $T\Delta s_{sl(LJ)}$ in Eq. (29) that

$$T\Delta s_{sl(LJ)}$$
$$\equiv \frac{A}{k_B T}\left[\int_{\kappa_0}^{\kappa}\kappa'\left(\overline{u_{sl(LJ)}^0 \cdot u_{sl(LJ)}^0} - \overline{u_{sl(LJ)}^0} \cdot \overline{u_{sl(LJ)}^0}\right)_{\lambda=0}d\kappa'\right.$$
$$\left. + \kappa\int_0^{\lambda}\left(\overline{u_{sl(C)}^0 \cdot u_{sl(LJ)}^0} - \overline{u_{sl(C)}^0}\,\overline{u_{sl(LJ)}^0}\right)_{\kappa}d\lambda\right]$$
$$= -\frac{A}{k_B T}\int_{\kappa_0}^{\kappa}\kappa'\sigma^2\left(u_{sl(LJ)}^0\right)_{\lambda=0}d\kappa'$$
$$- \frac{\kappa A}{k_B T}\int_0^{\lambda}\text{cov}\left(u_{sl(LJ)}^0, u_{sl(C)}^0\right)_{\kappa}d\lambda', \quad (30)$$

using the variance and covariance with respect to $u_{sl(LJ)}^0$ and $u_{sl(C)}^0$ given by

$$\sigma^2(u_{sl(LJ)}^0) \equiv \overline{(u_{sl(LJ)}^0)^2} - \overline{u_{sl(LJ)}^0}^2 \quad (31)$$

and

$$\text{cov}(u_{sl(LJ)}^0, u_{sl(C)}^0) \equiv \overline{u_{sl(LJ)}^0 u_{sl(C)}^0} - \overline{u_{sl(LJ)}^0} \cdot \overline{u_{sl(C)}^0}, \quad (32)$$

respectively. The second term of Eq. (30) can be further simplified, so that[41,42]

$$-\frac{\kappa A}{k_B T}\int_0^{\lambda}\text{cov}\left(u_{sl(LJ)}^0, u_{sl(C)}^0\right)_{\kappa}d\lambda' = u_{sl(LJ)}(\kappa, \lambda) - u_{sl(LJ)}(\kappa, 0),$$
$$(33)$$

which might appear surprising but is in fact inevitable, as it corresponds to the C-mp, where LJ interactions no longer explicitly depend on the coupling parameters and therefore the LJ component must be exactly energy-entropy compensating. This is equivalent to the exactly energy-entropy compensating liquid-liquid interactions discussed in the context of Eq. (7) in the Introduction section. On the other hand, the Coulomb contribution $T\Delta s_{sl(C)}$ is given by the following:

$$T\Delta s_{sl(C)} \equiv -\frac{A}{k_B T} \int_0^\lambda \lambda' \sigma^2(u_{sl(C)}^0) d\lambda'. \qquad (34)$$

Note that this division of entropy is somewhat arbitrary because of the dependence on the integration path.

Figure 7 shows the LJ and Coulomb components of the entropy loss $-T[s_{sl}]_{(1,0)}^{(1,\lambda)} \equiv -T[s_{sl}(1,\lambda) - s_{sl}(1,0)]$ and average total solid-liquid energy $-\overline{u}_{sl}$ along the C-mp (κ,λ) between $(1,0)$ and $(1,2)$. The entropy loss LJ component was obtained from Eq. (33), while the corresponding Coulomb component was obtained from Eq. (34). Both were calculated through numerical integration with keeping $\kappa = 1$. We confirmed that the entropy difference obtained by Eq. (27) corresponded to the previous result shown in the left panel of Fig. 3 calculated by Eq. (21). Note also that similar to Eq. (29), the relation $-\overline{u}_{sl} = -\overline{u}_{sl(LJ)} - \overline{u}_{sl(C)}$ holds for the average total solid-liquid energy, which is superimposed as a dashed line. As the coupling parameter λ increased, the Coulomb component of average total solid-liquid energy $-\overline{u}_{sl(C)}$ increased as easily expected, while the LJ component $-\overline{u}_{sl(LJ)}$ was reduced. This was closely related to the density distributions and dipole orientation, respectively, in Figs. 4 and 6, showing that the orientation change that led to the position change of water molecules upon strengthening the Coulomb interaction was in fact disadvantageous in respect to the LJ interaction. Accordingly, the
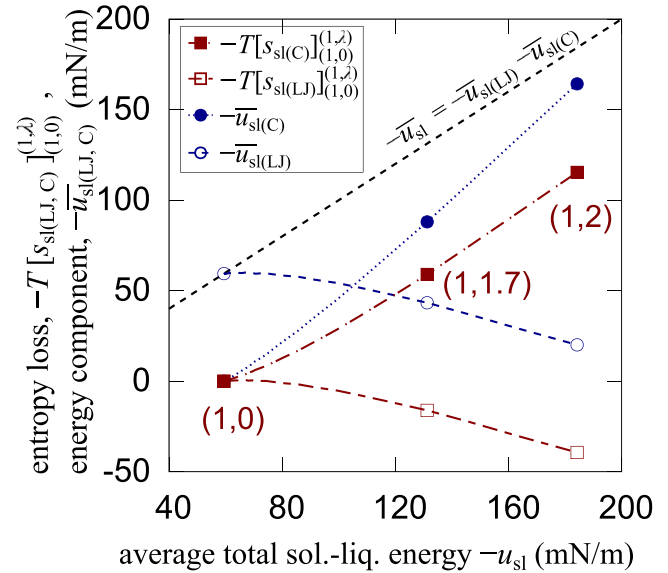

FIG. 7. Lennard-Jones (LJ) and Coulomb components of the entropy loss $-T[s_{sl}]_{(1,0)}^{(1,\lambda)} \equiv -T[s_{sl}(1,\lambda) - s_{sl}(1,0)]$ and average total solid-liquid energy $-\overline{u}_{sl}$ along the Coulomb modification phase (C-mp) of (κ,λ) between $(1,0)$ and $(1,2)$. (κ,λ) between $(1,0)$ and $(1,2)$. The entropy loss LJ component was obtained from Eq. (33), while the corresponding Coulomb component was obtained from Eq. (34).

changes in the entropy loss for the LJ and Coulomb components were in contrast: the entropy decreased for the Coulomb component, whereas it increased for the LJ component by strengthening the Coulomb interaction.

Finally, we tried to roughly estimate the change in the entropy loss without using thermodynamic integration. Considering that the entropy is a thermodynamic potential whose difference between two states is independent of the path, the entropy difference in Eq. (27) can be generally rewritten by an arbitrary line integral in the (κ,λ)-plane of

$$T\Delta s_{sl} = -\frac{A}{k_B T} \int_{(\kappa_0,0)}^{(\kappa,\lambda)} \left\{ \left[\kappa'\sigma^2\left(u_{sl(LJ)}^0\right) + \lambda'\mathrm{cov}\left(u_{sl(LJ)}^0, u_{sl(C)}^0\right) \right] d\kappa' + \left[\kappa'\mathrm{cov}\left(u_{sl(LJ)}^0, u_{sl(C)}^0\right) + \lambda'\sigma^2\left(u_{sl(C)}^0\right) \right] d\lambda' \right\}. \qquad (35)$$

As described in the Appendix, this entropy difference was separated into two terms as

$$T\Delta s_{sl} = T\Delta s_{sl}^{var} + T\Delta s_{sl}^{other}, \qquad (36)$$

where the first term directly corresponded to the variance of the average total solid-liquid energy

$$T\Delta s_{sl}^{var} \equiv -\frac{A}{2k_B T}\sigma^2(u_{sl}), \qquad (37)$$

which was calculated only with a single simulation at (κ,λ). On the other hand, the second term of the RHS of Eq. (36) could be calculated through the numerical integration as exemplified in Eq. (A6). Hence, a rough estimate of the entropy change was obtained as $T\Delta s_{sl}^{var}$ in Eq. (37) without numerical integration.

Figure 8 shows the comparison between the exact entropy loss $-T\Delta s_{sl}$ calculated by Eq. (21) or (27) and its rough estimate $-T\Delta s_{sl}^{var}$ calculated by Eq. (37) for the LJ-mp of (κ,λ) from $(\kappa_0, 0)$ to $(2, 0)$ and for the C-mp of (κ,λ) from $(1,0)$ to $(1,2)$. The entropy change was fairly well estimated by $-T\Delta s_{sl}^{var}$, indicating that the energy variance dominated a large part of the entropy change. It was also observed that the rough estimate also seemed to change linearly with $-\overline{u}_{sl}$. In addition, $-T\Delta s_{sl}^{var}$ qualitatively showed that for systems with the same solid-liquid energy, systems in the C-mp had a smaller work of adhesion than ones along the LJ-mp. Considering that no thermal integration and no parameters were needed for obtaining the rough estimate, this can be a valuable tool when a rough initial comparison of work of adhesion is needed. Of course further study is needed to see if this is applicable to a wide variety of systems and coupling parameters.
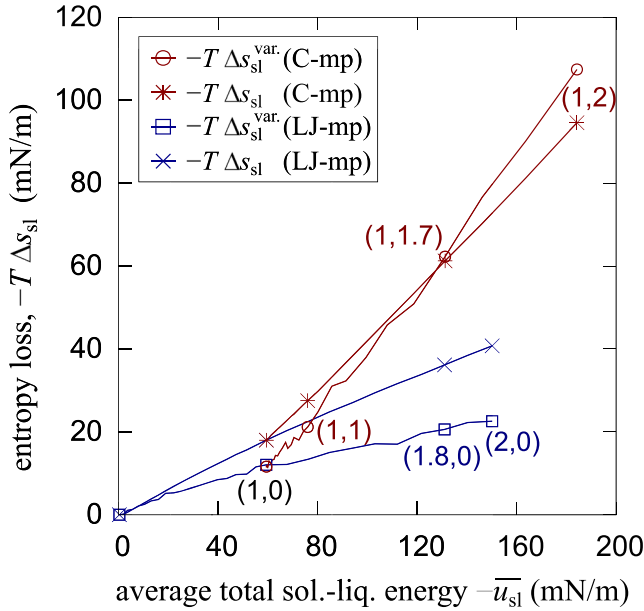
FIG. 8. Comparison between the exact entropy loss $-T\Delta s_{sl}$ calculated by Eqs. (21) or (27) and its rough estimate $-T\Delta s_{sl}^{var}$ calculated by Eq. (37) for the LJ modification phase (LJ-mp) of (κ, λ) between $(\kappa_0, 0)$ and $(2, 0)$ and for the Coulomb modification phase (C-mp) of (κ, λ) between $(1, 0)$ and $(1, 2)$. Corresponding values of (κ, λ) are shown for several points.

Equation (37) also gives a physical meaning behind the entropy change; i.e. systems with both LJ and Coulomb interactions have a broader interfacial energy distribution, which results in a larger entropy change. Note that the negative sign of Eq. (37) is due to the chosen direction of reversible process in this work. In the context of the definition of work of adhesion as work needed to separate liquid from solid, the sign would be positive and would indicate that the entropy gain due to separation is proportional to the interfacial energy variance at the start of separation.

IV. CONCLUDING REMARKS

We have performed molecular dynamics simulations of film systems containing a water-silica interface and extended the dry-surface method to compute work of adhesion in systems with long-range Coulomb interactions in the solid-liquid interface. An α-cristobalite $(10\bar{1})$ without silanol groups was chosen for the silica surface. The work of adhesion was increased by increasing both the LJ interaction strength and the silica charge, i.e., the silica polarity, which was in accordance with previously published works.[43,44] A linear relation at strong solid-liquid interactions was also shown between the solid-liquid energy and the work of adhesion, which resulted from the ratio between the change in the solid-liquid energy and the change in entropy caused by the solid-liquid interaction being mostly constant. This ratio, however, was different depending on the integration phase, and at same solid-liquid interfacial energies, systems with both LJ and Coulomb interactions had lower solid-liquid work of adhesion than systems with only LJ interaction, because of the bigger entropy change.

The relation between the solid-liquid entropy and energy variance was investigated, and it was shown that when increasing solid-liquid interaction strength at high solid-liquid energies, entropy loss was proportional to the negative of the variance change. This demonstrated that interfaces with Coulombic interaction had higher interfacial energy variations, which resulted in a bigger entropy loss. The following observation was made from this result: when in the context of work of adhesion as work needed to separate liquid from solid, systems with both LJ and Coulomb interactions at the solid-liquid interface have a broader distribution of interfacial energies, which results in higher entropy of adhesion, which then gets subtracted from the adhesion energy, resulting in lower work of adhesion. Finally, a rough way to estimate the work of adhesion for systems, which could fairly represent the qualitative feature of entropy change in the present system, was proposed, which does not require numerical integration in a parameter space.

APPENDIX: SEPARATION OF THE CHANGE IN SOLID-LIQUID ENTROPY

For the separation of the change in solid-liquid entropy, we start from the expansion of Eqs. (30) and (34). By applying partial integration, it holds regarding the first and second terms of the right-most hand side of Eq. (30) that

$$\int_{\kappa_0}^{\kappa} \kappa' \sigma^2 \left(u_{sl(LJ)}^0\right)_{\lambda=0} d\kappa' = \frac{1}{2}\left[\kappa'^2 \sigma^2 (u_{sl(LJ)}^0)_{\lambda=0}\right]_0^{\kappa} - \frac{1}{2}\int_0^{\kappa} \kappa'^2 \left.\frac{d\sigma^2(u_{sl(LJ)}^0)}{d\kappa'}\right|_{\lambda=0} d\kappa'$$

$$= \frac{1}{2}\sigma^2\left(u_{sl(LJ)}(\kappa, 0)\right) - \frac{1}{2}\int_0^{\kappa} \kappa'^2 \frac{d\sigma^2\left(u_{sl(LJ)}^0(\kappa', 0)\right)}{d\kappa'} d\kappa' \quad (A1)$$

and

$$\kappa \int_0^{\lambda} \text{cov}\left(u_{sl(LJ)}^0, u_{sl(C)}^0\right) d\lambda' = \kappa\left[\lambda' \text{cov}\left(u_{sl(LJ)}^0, u_{sl(C)}^0\right)\right]_0^{\lambda} - \kappa\int_0^{\lambda} \lambda' \frac{d\text{cov}\left(u_{sl(LJ)}^0, u_{sl(C)}^0\right)}{d\lambda'} d\lambda'$$

$$= \text{cov}\left(u_{sl(LJ)}, u_{sl(C)}(\kappa, \lambda)\right) - \kappa\int_0^{\lambda} \lambda' \frac{d\text{cov}\left(u_{sl(LJ)}^0, u_{sl(C)}^0\right)}{d\lambda'} d\lambda', \quad (A2)$$

respectively. In the same manner, the RHS of Eq. (34) is expanded by

$$\int_0^\lambda \lambda' \sigma^2(u_{\text{sl(C)}}^0) \mathrm{d}\lambda' = \frac{1}{2}\left[\lambda'^2 \sigma^2(u_{\text{sl(C)}}^0)\right]_0^\lambda - \frac{1}{2}\int_0^\lambda \lambda'^2 \frac{\mathrm{d}\sigma^2(u_{\text{sl(C)}}^0)}{\mathrm{d}\lambda'}\mathrm{d}\lambda'$$

$$= \frac{1}{2}\sigma^2\left(u_{\text{sl(C)}}(\kappa,\lambda)\right) - \frac{1}{2}\int_0^\lambda \lambda'^2 \frac{\mathrm{d}\sigma^2\left(u_{\text{sl(C)}}^0(\kappa,\lambda')\right)}{\mathrm{d}\lambda'}\mathrm{d}\lambda', \tag{A3}$$

respectively. A possible separation of entropy change $T\Delta s_{\text{sl}}$ into first term $T\Delta s_{\text{sl}}^{\text{var}*}$ and second term $T\Delta s_{\text{sl}}^{\text{other}*}$ with and without integration, respectively, as in Eq. (36), would be given by defining the former using the first terms of the right-most hand side of Eqs. (A1)–(A3) by

$$T\Delta s_{\text{sl}}^{\text{var}*} \equiv -\frac{A}{2k_\text{B}T}\left[\sigma^2\left(u_{\text{sl(LJ)}}(\kappa,0)\right) + 2\text{cov}\left(u_{\text{sl(LJ)}}, u_{\text{sl(C)}}(\kappa,\lambda)\right) + \sigma^2\left(u_{\text{sl(C)}}(\kappa,\lambda)\right)\right]. \tag{A4}$$

However, this separation is apparently path-dependent as obviously seen in the asymmetric form. Hence, we reformulate the first term into path-independent symmetric form by

$$T\Delta s_{\text{sl}}^{\text{var}} \equiv -\frac{A}{2k_\text{B}T}\left[\sigma^2\left(u_{\text{sl(LJ)}}(\kappa,\lambda)\right) + 2\text{cov}\left(u_{\text{sl(LJ)}}, u_{\text{sl(C)}}(\kappa,\lambda)\right) + \sigma^2\left(u_{\text{sl(C)}}(\kappa,\lambda)\right)\right]$$

$$= -\frac{A}{2k_\text{B}T}\left[\sigma^2\left(u_{\text{sl(LJ)}}(\kappa,\lambda) + u_{\text{sl(C)}}(\kappa,\lambda)\right)\right]$$

$$= -\frac{A}{2k_\text{B}T}\sigma^2\left(u_{\text{sl}}(\kappa,\lambda)\right), \tag{A5}$$

which corresponds to Eq. (37). Then the second term is given by

$$T\Delta s_{\text{sl}}^{\text{other}} = \frac{A}{2k_\text{B}T}\left[\int_{\kappa_0}^\kappa \kappa'^2 \frac{\mathrm{d}\sigma^2\left(u_{\text{sl(LJ)}}^0(\kappa',0)\right)}{\mathrm{d}\kappa'}\mathrm{d}\kappa' + 2\kappa \int_0^\lambda \lambda' \frac{\mathrm{d}\text{cov}\left(u_{\text{sl(LJ)}}^0, u_{\text{sl(C)}}^0\right)}{\mathrm{d}\lambda'}\mathrm{d}\lambda', + \int_0^\lambda \lambda'^2 \frac{\mathrm{d}\sigma^2\left(u_{\text{sl(C)}}^0(\kappa,\lambda')\right)}{\mathrm{d}\lambda'}\mathrm{d}\lambda'\right.$$

$$\left. + \sigma^2\left(u_{\text{sl(LJ)}}(\kappa,\lambda)\right) - \sigma^2\left(u_{\text{sl(LJ)}}(\kappa,0)\right)\right]$$

$$= \frac{A}{2k_\text{B}T}\left[\int_{\kappa_0}^\kappa \kappa'^2 \frac{\mathrm{d}\sigma^2\left(u_{\text{sl(LJ)}}^0(\kappa',0)\right)}{\mathrm{d}\kappa'}\mathrm{d}\kappa' + \int_0^\lambda \kappa^2 \frac{\mathrm{d}\sigma^2\left(u_{\text{sl(LJ)}}^0(\kappa,\lambda')\right)}{\mathrm{d}\lambda'}\mathrm{d}\lambda' + 2\int_0^\lambda \kappa\lambda' \frac{\mathrm{d}\text{cov}\left(u_{\text{sl(LJ)}}^0, u_{\text{sl(C)}}^0\right)}{\mathrm{d}\lambda'}\mathrm{d}\lambda',\right.$$

$$\left. + \int_0^\lambda \lambda'^2 \frac{\mathrm{d}\sigma^2\left(u_{\text{sl(C)}}^0(\kappa,\lambda')\right)}{\mathrm{d}\lambda'}\mathrm{d}\lambda'\right]. \tag{A6}$$

Since Eq. (A5) is path-independent, the rest of $T\Delta s_{\text{sl}}^{\text{other}}$ tentatively calculated by the line integral in Eq. (A6) via $(\kappa, 0)$ is also path-independent as long as the entropy in Eq. (35) satisfies the following totally differentiable condition:

$$\frac{\partial}{\partial \lambda'}\left[\kappa'\sigma^2\left(u_{\text{sl(LJ)}}^0\right) + \lambda'\text{cov}\left(u_{\text{sl(LJ)}}^0, u_{\text{sl(C)}}^0\right)\right]$$

$$= \frac{\partial}{\partial \kappa'}\left[\kappa'\text{cov}\left(u_{\text{sl(LJ)}}^0, u_{\text{sl(C)}}^0\right) + \lambda'\sigma^2\left(u_{\text{sl(C)}}^0\right)\right]. \tag{A7}$$

Equation (37) can also be derived by choosing a single straight integration path from $(\kappa_0, 0)$ to (κ, λ), on which the two parameters (κ', λ') are expressed by one variable $\chi \in [0, 1]$ as

$$(\kappa', \lambda') = \chi(\kappa, \lambda). \tag{A8}$$

On this path, the solid-liquid potential energy is given by

$$u_{\text{sl}}(\mathbf{\Gamma}, \chi) = \chi u_{\text{sl}}(\mathbf{\Gamma}, \kappa, \lambda), \tag{A9}$$

where $u_{\text{sl}}^{(\mathbf{\Gamma}, \kappa, \lambda)}$ is the potential energy calculated for given system coordinates using the potential parameters at (κ, λ). Then

the entropy change is calculated by

$$T\left[s_{\text{sl}}(\kappa, \lambda) - s_{\text{sl}}(\kappa_0, 0)\right] = -\frac{A}{k_\text{B}T}\int_0^1 \chi \sigma^2(u_{\text{sl}}^{(\kappa,\lambda)})\mathrm{d}\chi. \tag{A10}$$

By applying partial integration, $T\Delta s^{\text{var}}$ in Eq. (A5) is derived, while $T\Delta s^{\text{other}}$ is given by the following:

$$T\Delta s^{\text{other}} = \frac{A}{2k_\text{B}T}\int_0^1 \chi^2 \frac{\mathrm{d}\sigma^2(u_{\text{sl}}^{(\kappa,\lambda)})}{\mathrm{d}\chi}\mathrm{d}\chi. \tag{A11}$$

[1]T. Young, Philos. Trans. R. Soc. London **95**, 65 (1805).
[2]M. K. Chaudhury and G. M. Whitesides, Science **256**, 1539 (1992).
[3]S. Daniel, M. K. Chaudhury, and J. C. Chen, Science **291**, 633 (2001).
[4]Y. T. Cheng, D. E. Rodak, C. A. Wong, and C. A. Hayden, Nanotechnology **17**, 1359 (2006).
[5]Y. Son, C. Kim, D. J. Yang, and D. H. Ahn, Langmuir **24**, 2900 (2008).
[6]J. G. Park and M. F. Pas, J. Electrochem. Soc. **142**, 2028 (1995).
[7]J. G. Kirkwood and F. P. Buff, J. Chem. Phys. **17**, 338 (1949).
[8]M. J. P. Nijmeijer and J. M. J. van Leeuwen, J. Phys. A: Math. Gen. **23**, 4211 (1990).
[9]M. J. P. Nijmeijer, C. Bruin, A. F. Bakker, and J. M. J. van Leeuwen, Phys. Rev. A **42**, 6052 (1990).

[10] J. Z. Tang and J. G. Harris, J. Chem. Phys. **103**, 8201 (1995).

[11] S. Maruyama, T. Kuruashige, S. Matsumoto, Y. Yamaguchi, and T. Kimura, Microscale Thermophys. Eng. **2**, 49 (1998).

[12] P. van Remoortere, J. E. Mertz, L. E. Scriven, and H. T. Davis, J. Chem. Phys. **110**, 2621 (1999).

[13] S. K. Das and K. Binder, Europhy. Lett. **92**, 26006 (2010).

[14] D. Seveno, T. D. Blake, and J. De Coninck, Phys. Rev. Lett. **111**, 096101 (2013).

[15] S. Nishida, D. Surblys, Y. Yamaguchi, K. Kuroda, M. Kagawa, T. Nakajima, and H. Fujimura, J. Chem. Phys. **140**, 074707 (2014).

[16] D. Surblys, Y. Yamaguchi, K. Kuroda, M. Kagawa, T. Nakajima, and H. Fujimura, J. Chem. Phys. **140**, 034505 (2014).

[17] L. J. Schlangen, L. K. Koopal, M. A. C. Stuart, and J. Lyklema, Colloids Surf., A **89**, 157 (1994).

[18] M. Kanduč and R. R. Netz, J. Chem. Phys. **146**, 164705 (2017).

[19] F. Leroy and F. Müller-Plathe, Langmuir **31**, 8335 (2015).

[20] F. Leroy, S. Liu, and J. Zhang, J. Phys. Chem. C **119**, 28470 (2015).

[21] F. Leroy, J. Chem. Phys. **145**, 164705 (2016).

[22] M. J. Abraham, T. Murtola, R. Schulz, S. Páll, J. C. Smith, B. Hess, and E. Lindahl, SoftwareX **1-2**, 19 (2015).

[23] S. Plimpton, J. Comput. Phys. **117**, 1 (1995).

[24] F. Taherian, F. Leroy, and N. F. A. van der Vegt, Langmuir **29**, 9807 (2013).

[25] N. F. A. van der Vegt and D. Nayar, J. Phys. Chem. B **121**, 9986 (2017).

[26] A. R. Leach, *Molecular Modelling: Principles and Applications* (Prentice Hall, Harlow, UK, 2001), Vol. 2, p. 744.

[27] F. S. Emami, V. Puddu, R. J. Berry, V. Varshney, S. V. Patwardhan, C. C. Perry, and H. Heinz, Chem. Mater. **26**, 2647 (2014).

[28] W. Shinoda, M. Shiga, and M. Mikami, Phys. Rev. B **69**, 134103 (2004).

[29] G. Bussi and M. Parrinello, Phys. Rev. E **75**, 056707 (2007).

[30] Y. Wu, H. L. Tepper, and G. A. Voth, J. Chem. Phys. **124**, 024503 (2006).

[31] G. Raabe and R. J. Sadus, J. Chem. Phys. **134**, 234501 (2011).

[32] B. R. Brooks, R. E. Bruccoleri, B. D. Olafson, D. J. States, S. Swaminathan, and M. Karplus, J. Comput. Chem. **4**, 187 (1983).

[33] R. W. Hockney and J. W. Eastwood, *Computer Simulation Using Particles* (Taylor & Francis, Inc., Bristol, PA, USA, 1988).

[34] I. Yeh and M. L. Berkowitz, J. Chem. Phys. **111**, 3155 (1999).

[35] G. Bussi, D. Donadio, and M. Parrinello, J. Chem. Phys. **126**, 014101 (2007).

[36] J. E. Basconi and M. R. Shirts, J. Chem. Theory Comput. **9**, 2887 (2013).

[37] J. G. Kirkwood, J. Chem. Phys. **3**, 300 (1935).

[38] F. Sedlmeier, J. Janecek, C. Sendner, L. Bocquet, R. R. Netz, and D. Horinek, Biointerphases **3**, FC23 (2008).

[39] D. Surblys, Y. Yamaguchi, K. Kuroda, T. Nakajima, and H. Fujimura, J. Chem. Phys. **135**, 014703 (2011).

[40] C. E. Shannon, Bell Syst. Tech. J. **27**, 379 (1948).

[41] H. Yu and M. Karplus, J. Chem. Phys. **89**, 2366 (1988).

[42] C. Peter, C. Oostenbrink, A. van Dorp, and W. F. van Gunsteren, J. Chem. Phys. **120**, 2652 (2004).

[43] C. Wang, B. Zhou, Y. Tu, M. Duan, P. Xiu, J. Li, and H. Fang, Sci. Rep. **2**, 358 (2012).

[44] N. Giovambattista, P. G. Debenedetti, and P. J. Rossky, J. Phys. Chem. B **111**, 9581 (2007).